




System and path planning algorithm for low-kV X-ray free-form surface irradiation

Andreas Rothfuss¹  | Oliver Oesterle¹ | Daniel Bürgy² | Charles Nwankwo² |
Frank Schneider² | Auguste van Poelgeest¹ | Frederik Wenz² |
Jan Stallkamp¹ | Sven Clausen²

¹Project group for Automation in Medicine and Biotechnology, Fraunhofer IPA, Mannheim, Germany

²Department of Radiotherapy and Radiation Oncology, Medical Faculty Mannheim at Heidelberg University, Mannheim, Germany

Correspondence

Andreas Rothfuss, Project group for Automation in Medicine and Biotechnology, Fraunhofer IPA, Mannheim, Germany.
Email: andreas.rothfuss@ipa.fraunhofer.de

Funding information

German Federal Ministry for Education and Research, Grant/Award Number: 13GW0090; European Community's Seventh Framework Program, Grant/Award Number: FP7/2007-2013; Research, Technological Development and Demonstration; 602306

Abstract

Objective: Intraoperative radiotherapy (IORT) after surgical resection using a low-kV-X-ray source is a proven method used in cancer treatment. However, the shape and size of the targeted surface area are limited to the size of the available applicators. This can lead to nonconformal and therefore suboptimal treatment for many patients.

Methods: A system is proposed comprising an X-ray source with an applicator for surface irradiation mounted on a robotic arm. This is controlled by an algorithm designed for planning the required continuous path, enabling irradiation of any desired shape with a controlled dose distribution.

Results: The system is shown to be capable of irradiating areas composed of rectangles on a flat surface with a homogeneity index of less than 7% inside the targeted area.

Conclusion: The presented results demonstrate the potential of the proposed setup to eliminate the current limitations, leading to better treatment of patients.

KEYWORDS

brachytherapy, continuous path planning, iort, modeling, simulation, x-ray

1 | INTRODUCTION

Cancer-associated mortality is a leading cause of death worldwide.^{1,2} Approximately 50% of all cancer patients receive radiotherapy at least once during the course of their disease.³ In recent years, developments of new techniques such as low-kV intraoperative radiotherapy (IORT) have led to several new therapeutic options for cancer patients. Currently, IORT is primarily (and increasingly) used in breast cancer patients.⁴ Primary treatment of breast cancer with IORT is a straightforward approach because of the spherical (typically not irregular) wound cavity.⁵ In a recently published analysis, 78.7% of all IORTs were performed in breast cancer patients, followed by 8.9% in patients with rectal carcinoma. Sarcoma patients accounted for a share of 3.6% of all IORT procedures.⁴ IORT is an efficient method for tumour control in patients where a residual tumour cannot be removed by surgery (R1 or R2 resection).^{6,7} Owing to its radiation hygiene and biology the INTRABEAM® system by Carl Zeiss Meditec AG is ideally suited for

this kind of therapy.⁸ With today's systems, the irradiation of only a flat, circular area with a diameter up to 6 cm is possible. More complex or larger target areas cannot be irradiated by IORT with a reproducibly controlled dose distribution. Larger areas cannot be covered evenly since a manual shift of the applicator position would lead to unpredictable dose overlaps and peaks. Thus, the irradiated area is limited because the radiation source must be static. Many patients who could potentially benefit from this kind of therapy are excluded by these limitations. The same problem exists in the treatment of cutaneous metastases by means of IORT. Skin metastases are associated with significant morbidity in cancer patients. Ulcerated lesions may lead to bleeding and local infections.^{9,10} Furthermore, the patient's quality of life is reduced by cutaneous metastases¹¹; the causes are the complications mentioned above and/or the mental burden of the visibility of the disease. Although there are various noninvasive methods for the treatment of skin metastases,¹² a complete remission is achieved only in a minority of cases. Several robotic brachytherapy systems have been

This is an open access article under the terms of the Creative Commons Attribution-NonCommercial-NoDerivs License, which permits use and distribution in any medium, provided the original work is properly cited, the use is non-commercial and no modifications or adaptations are made.

© 2018 The Authors The International Journal of Medical Robotics and Computer Assisted Surgery Published by John Wiley & Sons Ltd.

described.^{13,14} Most of the systems have been developed for source placement in the prostate or in the lung. To the best of our knowledge, no robotic systems for the low-kV INTRABEAM[®] system have been described. Besides the treatment of skin metastases, robotic guidance could improve the dose distribution of the INTRABEAM[®] system in intraoperative scenarios with irregular treatment volumes as seen in sarcoma surgery.¹⁵ Due to the favorable biological and physical properties of the low-kV radiation, the IORT system would be a useful addition to the existing treatment methods, as long as it were possible to achieve a predictable and reproducible dose distribution on the irradiated surface.

1.1 | System goals

The objective of the proposed system is the implementation of a robot-assisted radiation therapy device to optimize IORT for sarcoma and cutaneous metastases by uniform irradiation of larger, irregularly shaped and uneven surfaces.

The maximum range for the target dose is defined by a realistic treatment dose for the targeted surface. The prescription dose can be derived from related treatments such as the TARGIT treatment for breast cancer as described in.¹⁶ In complex intraoperative settings, organs at risk, such as nerves, may limit the possible dose that can be applied to the target structure. Manually guided IORT at the discretion of the treating radiation oncologist is not reproducible and dose distributions can only be estimated. For our robotic approach, we applied a margin to the target dose that is mainly derived from geometrical uncertainties due to the high dose gradient of low-kV radiation. For example, a geometrical error of 1 mm leads to a dose error of up to 15% depending on the gradient of the dose fall-off in the specific location. The overall time for planning and the delivery of the prescribed dose itself can also be derived from the treatment time found acceptable in.¹⁶

This leads to the following required specifications:

- The range for the maximum target dose is 3 to 10 Gy.
- The margin for the target dose deviation is $\pm 10\%$.
- The planning time combined with the treatment time should be less than one hour.

1.2 | Proposed system set-up

The proposed system consists of a low-kV X-ray source, a beam-forming applicator for the X-ray source, a robotic arm and a path planning system. The X-ray source with its applicator is mounted on the robot's flange and thereby enables the surface irradiation. The system setup is shown in figure 1. The robot path leading to a controlled surface dose is computed by the path planning system, based on the surface itself, the radiation characteristics of the X-ray sources and a predefined plan for the target dose and the air-gap between the X-ray source and the surface. The latter is introduced to fulfill the desire for an irradiation system without direct patient contact to prevent injury to the patient and to enable a much easier risk assessment for the human-machine interaction.

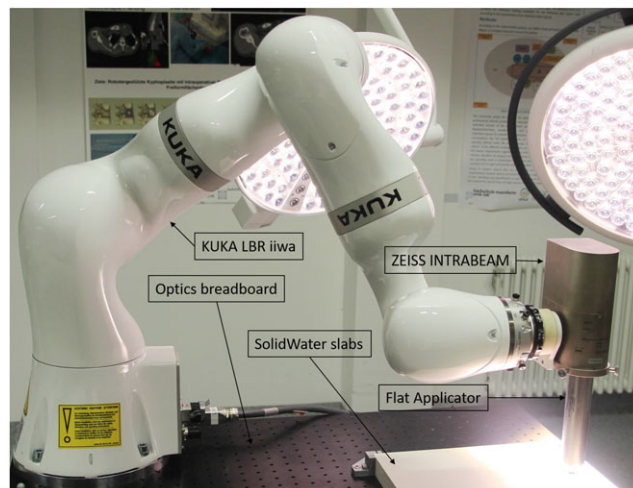


FIGURE 1 System set-up with Zeiss INTRABEAM[®] mounted on the Kuka LBR iiwa

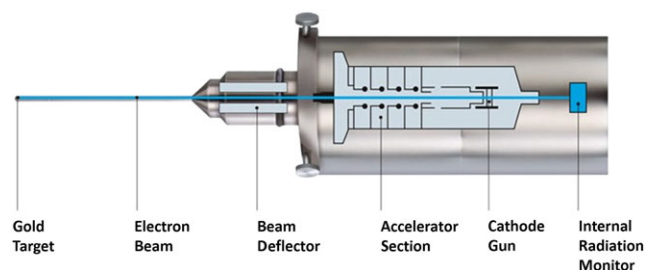


FIGURE 2 INTRABEAM[®] XRS 4 X-ray source with its principal components and their positions,¹⁷ © Carl Zeiss Meditec AG

2 | MATERIALS: COMPONENTS

The resulting surface dose is strongly dependent on the characteristics of the X-ray source and the robotic arm. For the X-ray source this concerns mostly its radiation characteristics, whereas the motion characteristics of the robotic arm have a significant impact on the resulting dose and therefore the path planning. The following section will present the components' characteristics in detail in order to enable the definition of a simulation model enabling the simulation of the system's behaviour and thus the desired path planning.

2.1 | X-ray source

The low-kV X-ray source for the proposed set-up is the INTRABEAM[®] with a Flat applicator, both by Carl Zeiss Meditec AG.

2.1.1 | X-ray generation

The X-rays emitted by the XRS 4 are generated by a beam of accelerated electrons hitting a gold target. A schematic drawing of the source is depicted in figure 2.

2.1.2 | Beam shaping

As the X-ray photons are emitted in random directions during the electron deceleration, the bare probe's radiation characteristic is nearly spherical. This means that isodose surfaces are spherical surfaces with the probe's tip as the centre. This would cause a dose distribution unsuitable for surface irradiation, so the dose distribution needs to be changed. Therefore, an applicator is placed around the probe of the X-ray source as described in.¹⁸ This applicator is made of metal, absorbing most of the radiation except for the radiation directed towards the circular window pointing away from the source. This results in a cone-shaped beam distribution. A flattening filter is placed inside this window. It is responsible for shaping the dose rate distribution inside the beam cone, such that a nearly flat dose rate distribution is apparent at a specific depth.

2.1.3 | Beam characteristics

The dose rate distribution of the X-ray sources with the Flat applicator described above can be seen in figure 3. In the far field (outside 6 mm depth) the isodose surfaces are spherical, as without any applicator, with a centre near the tip of the probe. In the near field (inside 2 mm depth) the isodose surfaces are spherical as well, but with a centre beyond the probe or applicator. In between near and far field, the isodose surfaces are close to planes.

2.2 | Robotic system

The robotic arm used to move the X-ray source must fulfill two main requirements besides being able to manage the weight of the source. First, the robotic arm needs to be able to operate in cooperation with humans without requiring a protective fence because the targeted application requires the robot arm to move a distance of a few millimetres from the surface of a surgical wound cavity. Secondly, the robot's motions should be as precise as possible to minimize the deviation from the planned target surface dose. To fulfill these requirements, of which the capability to operate in nearly direct contact with humans is by far

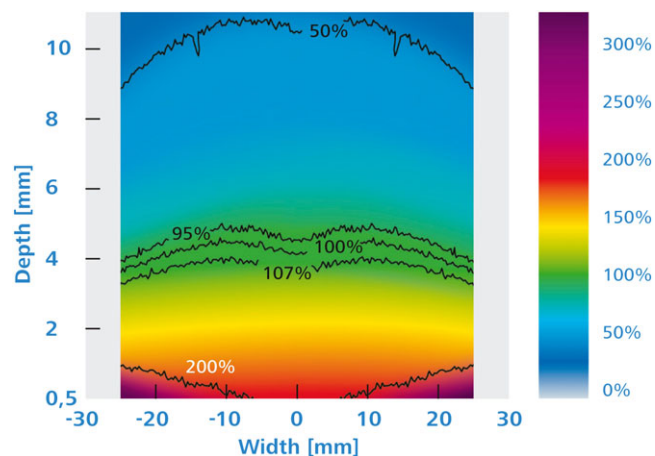


FIGURE 3 INTRABEAM® depth dose with a Flat applicator,¹⁹ © Carl Zeiss Meditec AG

the harder to achieve, a KUKA LBR iiwa was used to implement the robotic movements.

2.2.1 | Motion model

In order to have an accurate representation of the source's position $\vec{x}_Q(t)$ at any time t , the robot's motion characteristics need to be included in the simulation model. The most important of those are the motion characteristics associated with

- linear Cartesian motions with constant speed,
- blend up motions when starting a motion from a complete stop,
- blend down motions when ending a motion in a complete stop, and
- blend over motions when changing direction between two linear Cartesian motions with constant speed.

The results of measurements of linear motions with the KUKA LBR iiwa with the INTRABEAM® attached to its flange show a maximal Cartesian error of 0.2 mm. Because of this, linear Cartesian motions with constant speed are modeled as motions with constant speed and direction because the inaccuracy of those motions is too small to have a quantifiable effect on the resulting target surface dose D . The inaccuracy is also assumed to be random, hence it cannot be included in the model for the planning system. Therefore, the motions can be expressed as

$$\vec{x}_Q(t_m) = \vec{x}_s + \vec{v}t_m, \quad 0 \leq t_m \leq t_e \quad (1)$$

where

$$\vec{v} = \frac{\vec{x}_e - \vec{x}_s}{|\vec{x}_e - \vec{x}_s|} v$$

with the starting point \vec{x}_s , the end point \vec{x}_e , the motion speed v and the time t_e at which the end point is reached.

Blend up and down motions are described using polynomial blending functions, as described in²⁰ using fifth-order polynomials

$$\vec{x}_Q(t_m) = \vec{b}_0 + \vec{b}_1 t_m + \vec{b}_2 t_m^2 + \vec{b}_3 t_m^3 + \vec{b}_4 t_m^4 + \vec{b}_5 t_m^5 \quad (2)$$

where the polynomial coefficients are defined by the starting and ending positions, velocities and accelerations of the blend trajectory. With these parameters defined, the coefficients can be computed by solving a linear equation as defined in.²⁰

Blend over motions are defined by trigonometric blending functions

$$\vec{x}_Q(t_m) = -\vec{A}_{max} \frac{T^2}{\pi^2} \sin\left(\frac{\pi}{T} t\right) + \vec{v}_0 t_m + \vec{x}_Q(t_0). \quad (3)$$

All of those modelled motion characteristics have been parametrized to fit the motion characteristics of the commercial robot system. An evaluation of computed and recorded robotic motions has yielded a sufficient representation of the actual motion characteristics of the robot by the model.

3 | METHODS: PLANNING SYSTEM

The planning system's purpose is to plan a path for the radiation source with the goal of achieving a resulting dose on the target surface that fits the target dose. In order to achieve this goal, we have to be able to

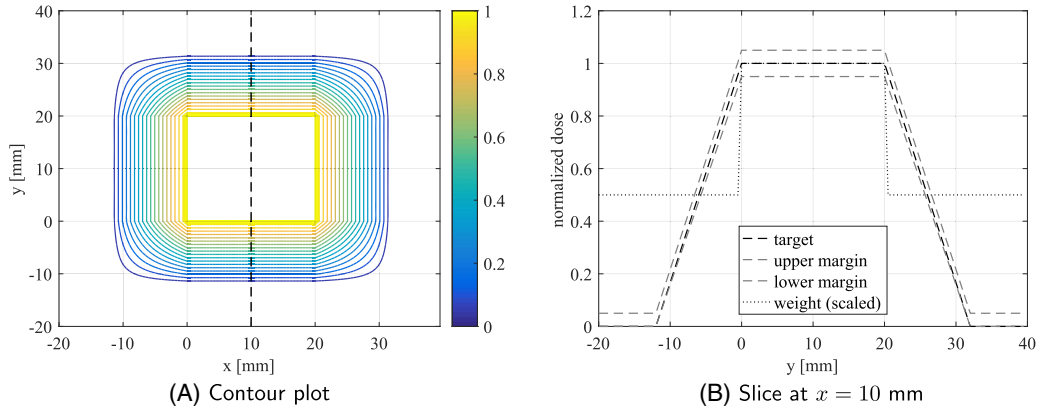


FIGURE 4 Target dose D_t for a 20 mm by 20 mm field with margins. The target dose is constant inside the field and outside the field with spatial margins (12 mm). In between, the target dose is interpolated from values inside and outside. In figure 4b the target dose (black, —) is between the upper and lower margins (grey, - -), which are computed from the target dose ($\pm 5\%$ inside the field, $+5, -0\%$ outside the margins). The weight (black, · · ·) is scaled to the maximal target dose

simulate the resulting dose based on the source's radiation characteristics and its path. Therefore, a simulation for the resulting target surface dose has been implemented.

3.1 | Target surface dose

The radiation source's dose rate can be described by a dose kernel. This dose kernel describes the dose rate $\dot{D}(t, \vec{x})$ at time t for any position \vec{x} where x_{DK} is the position relative to the source's position $\vec{x}_Q(t)$,

$$\dot{D}(t, \vec{x}) = \dot{D}(\vec{x}_{DK} - \vec{x}_Q(t)). \quad (4)$$

The target surface dose $D(t, \vec{x})$ at any point \vec{x} on the target surface for any given time t is given by integration of (4):

$$D(t, \vec{x}) = \int_{t_0}^t \dot{D}(\vec{x}_{DK} - \vec{x}_Q(\tau)) d\tau + D(t_0, \vec{x}). \quad (5)$$

3.2 | Definition of the problem

With these models for the target surface dose and the source motion, the path planning problem can be expressed as an optimization problem with the objective of finding the source path that minimizes the difference between target dose and actual dose.

The minimization problem is defined as

$$\begin{aligned} & \underset{\vec{x}_Q}{\text{minimize}} && f(D_d(T, \vec{x})) \\ & \text{subject to} && \vec{x}_Q \in \mathcal{C}^2 \end{aligned} \quad (6)$$

where $f(D_d)$ is the positive definite cost function defining the cost of a deviation between target dose D_t and actual dose,

$$D_d(T, \vec{x}) = D_t(T, \vec{x}) - D(T, \vec{x}),$$

in short $D_d(\vec{x})$. This cost function was chosen as

$$f(D_d(\vec{x})) = \int_A w(\vec{x}) f_i(D_d(\vec{x})) d\vec{x} \quad (7)$$

where $f_i(D_d(\vec{x}))$ is made to distinguish between areas where the deviation D_d is inside or outside predefined margins:

$$f_i(D_d(\vec{x})) = \begin{cases} D_d(\vec{x})^2 & D_d(\vec{x}) \text{ inside margins} \\ 2D_d(\vec{x})^2 & D_d(\vec{x}) \text{ outside margins.} \end{cases}$$

Equation 7 can also be expressed, for an area with discrete pixels, as

$$f(D_d(\vec{x})) = \sum_{x_{ij} \text{ in } A} w(x_{ij}) f_i(D_d(x_{ij})).$$

An example for a target dose D_t for a target field of 20 mm by 20 mm and a target value of 1 is depicted in figure 4. Inside the target field, the target value is constant and the upper and lower dose margins are dependent on the target value ($\pm 1\%$). Outside the target field, a linear gradient is assumed because the target with dose margins is still dependent on the target value. Outside this spatial margin, a target value of 0 is assumed, while an upper dose margin of 1% of the maximum target value for the field is assumed to account for scattered radiation.

3.3 | Definition of the pattern

In order to simplify the minimization problem (6), the source's movement \vec{x}_Q is restricted to two particular patterns.

While both patterns are defined as movements in a plane parallel to the targeted surface with a constant distance to the former, the parallel paths pattern (PPP) consists of parallel, equidistant segments connected by blend motions (figure 5). Each segment has the same motion speed. This pattern is defined by six scalar parameters:

- $v \in \mathbb{R}^+$: motion speed
- $n \in \mathbb{N}^+$: number of path segments
- $d \in \mathbb{R}^+$: distance between segments
- $x_s, y_s \in \mathbb{R}$: x and y components of the start point
- $l \in \mathbb{R}$: length of the segments.

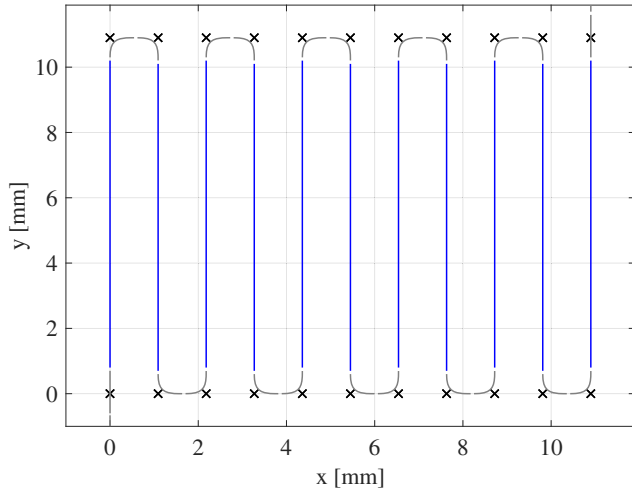


FIGURE 5 Paths of a PPP for $x_s = y_s = 0$ mm, $d = 1.09$ mm, $n = 11$ and $y_e = 10.9$ mm with defining frames (black, x), segments (blue) and blends (grey)

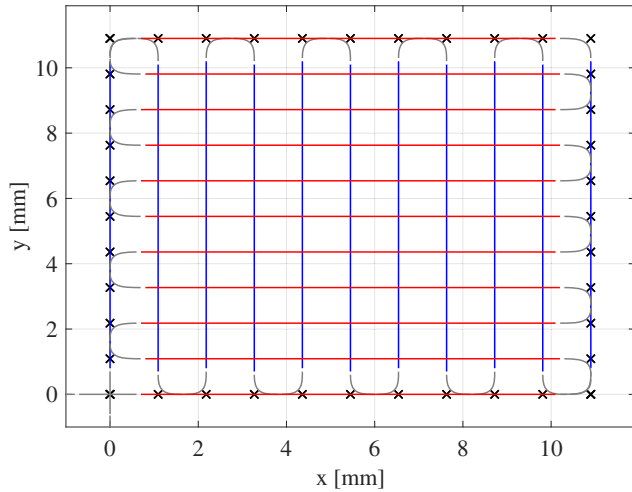


FIGURE 6 Paths of a CPPP for $x_s = y_s = 0$ mm, $d_1 = d_2 = 1.09$ mm and $n_1 = n_2 = 11$ with defining frames (black, x), first PPP segments (blue), second PPP segments (red) and blends (grey)

A PPP that started at its southwest corner (which can be assumed without loss of generality) can end in its southeast and northeast corners, depending on the parity of the number of major paths.

The crossed parallel paths pattern (CPPP) consists of two perpendicular PPPs (figure 6) and is defined by eight parameters:

- $v_1, v_2 \in \mathbb{R}^+$: motion speed for each PPP
- $n_1, n_2 \in \mathbb{N}^+$: number of segments for each PPP
- $d_1, d_2 \in \mathbb{R}^+$: distance between segments for each PPP
- $x_s, y_s \in \mathbb{R}$: x and y components of the start point.

A CPPP that started at the southwest corner (which can also be assumed without loss of generality) can end in each of its corners.

With these patterns, any exit direction is possible for any rectangular field. This enables the pattern to be chosen in order to fit the current need for concatenation.

Applying these patterns with (1), (2) and (3) to the minimization problem (6), this becomes

$$\underset{(x_s, y_s, y_e, n, d, v)}{\text{minimize}} \sum_{x_{ij} \text{ in } A} w(x_{ij}) f_i(D_d(x_{ij})) \quad (8)$$

$$\text{subject to } (x_s, y_s, y_e) \in \mathbb{R}, n \in \mathbb{N}^+, (d, v) \in \mathbb{R}^+$$

for a PPP and

$$\underset{(x_s, y_s, n_k, d_k, v_k)}{\text{minimize}} \sum_{x_{ij} \text{ in } A} w(x_{ij}) f_i(D_d(x_{ij})), k \in (1, 2) \quad (9)$$

$$\text{subject to } (x_s, y_s) \in \mathbb{R}, n_k \in \mathbb{N}^+, (d_k, v_k) \in \mathbb{R}^+$$

for a CPPP and with

$$f_i(D_d(x_{ij})) = \begin{cases} D_d(x_{ij})^2 & D_d(x_{ij}) \text{ inside margins} \\ 2D_d(x_{ij})^2 & D_d(x_{ij}) \text{ outside margins.} \end{cases}$$

These are solvable for rectangular target areas using a solver for mixed integer optimization problems for nonlinear objective functions such as the genetic algorithm implemented in MATLAB[®].²¹ However, the time needed to compute the optimal solution is too long to comply with the system goals, due to the significant amount of time needed to compute the solution for each target surface dose $D(T)$.

3.4 | Solution to the problem

In order to make the optimization problem (6) solvable in an acceptable computation time, the symmetry in the solution of the target surface dose due to linear motions with constant speed is used.

Figure 7 shows the resulting target surface dose for a single linear path D_{SP} starting at $\vec{x}_s = [0, -25]$ and ending at $\vec{x}_s = [0, 25]$. In the y interval $[-15, 15]$ the dose is constant for a constant x. The gradients outside this interval occur because of shorter irradiation times due to the start and endpoint of the path and the acceleration. Therefore, a slice at one constant y is representative of the whole y interval and can be used to find solutions to the optimization problem for the parameters x_s, n, d and v , because the resulting dose D is inversely proportional to the speed v . The resulting 1-dimensional dose $D_1(x)$ for a PPP along its major direction is

$$D_1(x) = D_{i1}(x) + \sum_{i=0}^{n-1} D_{SP}(x - x_s + id, 0) \frac{1}{v}$$

with the initial 1-dimensional dose D_{i1} .

This simplifies the minimization problem in its discrete form to

$$\underset{(x_s, n, d, v)}{\text{minimize}} \sum_{x_i} w(x_i) f_i(D_{i1}(x_i) - D_1(x_i)) \quad (10)$$

$$\text{subject to } x_s \in \mathbb{R}, n \in \mathbb{N}^+, (d, v) \in \mathbb{R}^+$$

with

$$f_i(D_{d1}(x_i)) = \begin{cases} D_{d1}(x_i)^2 & D_{d1}(x_i) \text{ inside margins} \\ 2D_{d1}(x_i)^2 & D_{d1}(x_i) \text{ outside margins.} \end{cases}$$

The simplified form of the minimization problem (10) can be solved by the genetic algorithm in a reasonable time.

The previously unknown values for the parameters y_s and y_e of a PPP could be obtained by solving (8) while fixing the parameters x_s, n, d and v . However, this would not sufficiently reduce the computation time. Once again, making use of the symmetry of the solution of (5) for a PPP with assumed values for y_s and y_e has the potential to reduce

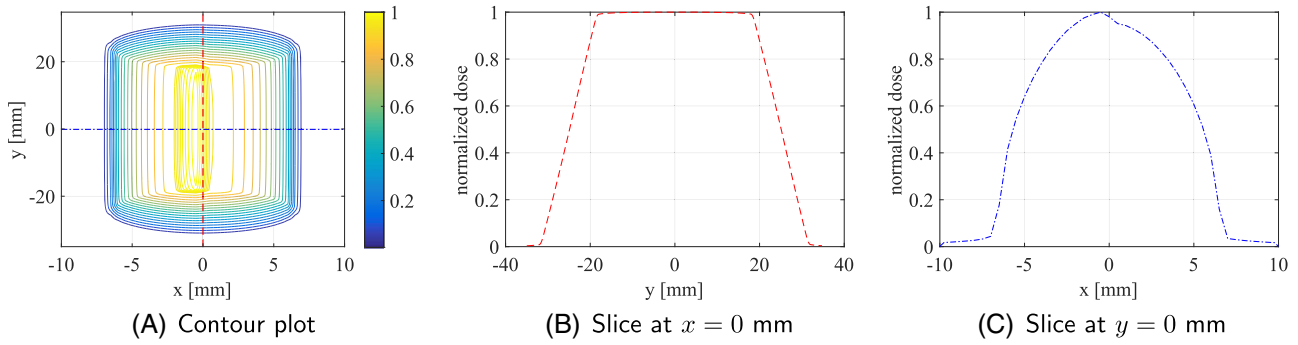


FIGURE 7 Resulting dose $D_{sp}(T)$ for a single linear path from $\bar{x}_s = [0, -25]$ to $\bar{x}_e = [0, 25]$. The resulting dose $D_{sp}(T)$ is constant for any given value of x inside the y interval $[-15, 15]$, enabling the use of the symmetry about $y = 0$ to speed up the computation

the computation time significantly. A change in the parameter y_s can be achieved by shifting the resulting dose D in the y direction. A change in the parameter y_e can be achieved by shrinking or expanding the constant part in the middle (around $\frac{y_e - y_s}{2}$). These two operations reduce the computation time for the solution of (8) and yield, together with the method described above, a solution for (8) in a reasonable time.

The same logic applies to the simplification of the minimization problem (9). In the case of a CPPP, the minimization problem (10) has to be solved twice: once for the first major direction with a halved target dose D_{t1} and the parameters x_s, n_1, d_1 and v_1 , and then again with an initial dose D_{10} for the second major direction and the parameters n_2, d_2 and v_2 . The initial dose D_{10} for the second solution of (10) can be obtained by computing the solution of (5) for a PPP as described above.

3.5 | Adjoining fields

For fields composed of several rectangular fields, it is simple to start with the rectangular field furthest to the left. With the solution for this field's target surface dose, the initial dose for any field adjoining this field can be determined. The solution for the first of the adjacent fields can be computed by using either a PPP or a CPPP depending on the path exit requirements for any further fields. With this solution, the initial field for any field adjacent to the second can be computed. This process goes on, again using PPPs or CPPPs defined by the current need, until the solution for the last rectangular field has been computed.

3.6 | Experimental set-up

An experiment has been conducted in order to test the model for the simulation of the target surface dose and the source motion. The experimental set-up, which can be seen in figure 1 and,²² consists of a Kuka LBR iiwa mounted on an optics breadboard, a holder for the INTRABEAM® X-ray source, to mount it on the robot's flange and a Gafchromic EBT-3® (EBT-3) radiation-sensitive film, which is placed on top of three SolidWater slabs, which are in turn placed on the optics breadboard. In preparation for the experimental validation, radiation source paths for two different shapes with a constant target dose and a PPP and a CPPP each have been computed. The paths have been transferred from the planning system to the robot using a csv file defining

the frames, which define the pattern path. First, the paths have been executed once, using a superimposed force normal to the SolidWater slabs and the robot's force-sensing capabilities to measure the actual position of the target surface in the robot's coordinates. These measurements were then used to suppress the known absolute accuracy of the robot and the unknown exact thickness of the SolidWater slabs. After realizing this setup, the radiation source was turned on and subsequently the robot motion was started. Once the trajectory of the source was completed, the source was turned off. The irradiated EBT-3 films were then calibrated to absolute dose using reference films with known irradiated dose measured by an ionization chamber (PTW Freiburg 23342) with the same setup but constant position. The calibration method is explained more detailed by Kalkan *et al.*²³

4 | RESULTS

4.1 | Planning results

Three different paths have been planned for the experimental validation of the presented models and methods: 2 for a rectangular field with a PPP and a CPPP path and 1 for an 'L'-shaped field with a PPP. The parameter sets for the computed patterns are summarized in table 1. Each field is characterized by the mean value, the standard deviation

TABLE 1 Parameter sets for the planned patterns

Field	Pattern	Parameters	
Rectangular	PPP	$v = 1.791 \text{ mm s}^{-1}$	$n = 64$
		$d = 1.125 \text{ mm}$	$x_s = -5.361 \text{ mm}$
	CPPP	$y_s = -5.744 \text{ mm}$	$y_e = 51.503 \text{ mm}$
		$v_1 = 2.798 \text{ mm s}^{-1}$	$n_1 = 50$
'L' shape	CPPP	$d_1 = 1.440 \text{ mm}$	$x_s = -5.202 \text{ mm}$
		$v_2 = 2.107 \text{ mm s}^{-1}$	$n_2 = 31$
		$d_2 = 1.897 \text{ mm}$	$y_s = -4.7515 \text{ mm}$
	PPP(1)	$v = 1.397 \text{ mm s}^{-1}$	$n = 22$
		$d = 1.430 \text{ mm}$	$x_s = -4.744$
		$y_s = -5.109 \text{ mm}$	$y_e = 63.506 \text{ mm}$
PPP(2)	$v = 1.408 \text{ mm s}^{-1}$	$n = 28$	
	$d = 1.4279 \text{ mm}$	$x_s = 6.777 \text{ mm}$	
	$y_s = -5.560 \text{ mm}$	$y_e = 45.499 \text{ mm}$	

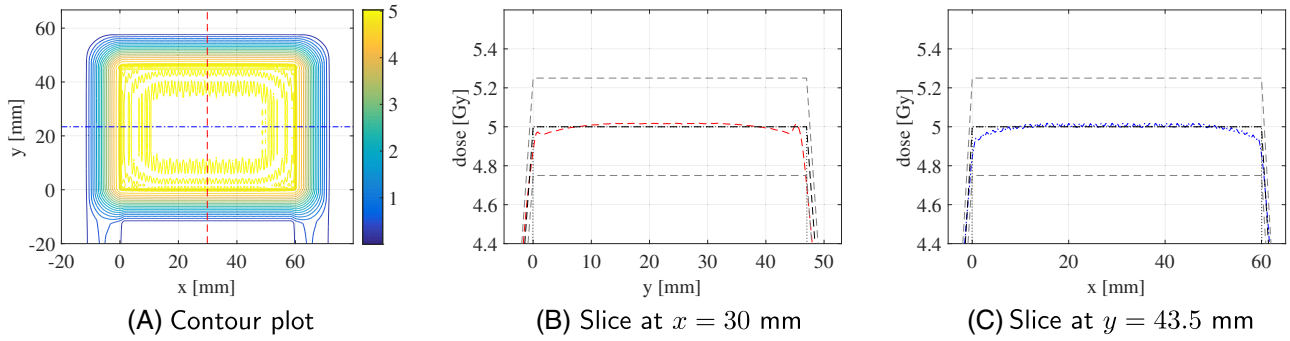


FIGURE 8 Resulting dose $D(T)$ for a planned source path for a rectangular field of 60 mm by 47 mm using a PPP. Figures 8b and 8c show the resulting dose (red, —) and (blue, - · -) with the target dose as shown in Figure 4b zoomed in to better show the resulting dose inside the field

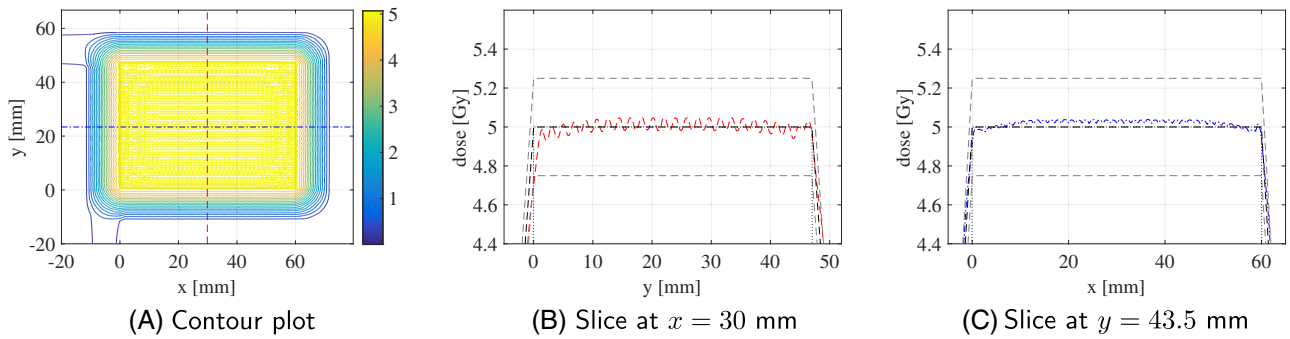


FIGURE 9 Resulting dose $D(T)$ for a planned source path for a rectangular field of 60 mm by 47 mm using a CPPP. Figures 9b and 9c show the resulting dose (red, —) and (blue, - · -) with the target dose as shown in Figure 4b zoomed in to better show the resulting dose inside the field

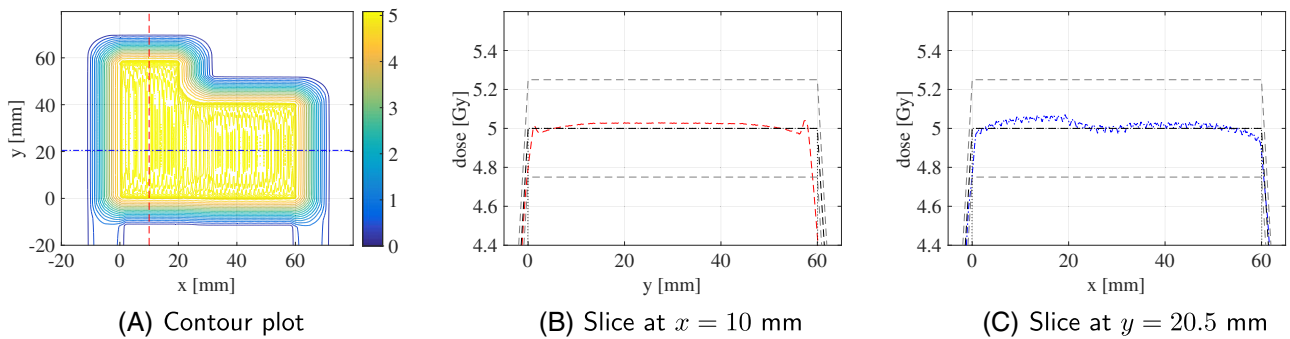


FIGURE 10 Resulting dose $D(T)$ for a planned source path for an 'L'-shaped field of 60 mm by 20 mm and of 40 mm by 41 mm using two PPPs. Figures 10b and 10c show the resulting dose (red, —) and (blue, - · -) with the target dose as shown in Figure 4b zoomed in to better show the resulting dose inside the field

and the homogeneity inside the target field. As a homogeneity measure we used the homogeneity index as described in formula D of ²⁴:

$$HI = \frac{D_5 - D_{95}}{D_p} \times 100$$

where D_5 and D_{95} are the minimum dose in 5% and 95% of the target volume with the highest actual dose and D_p is the prescribed dose. The ideal value is zero when D_5 and D_{95} are equal.

4.1.1 | Rectangular field

The rectangular field is the simplest possible shape for the presented path planning algorithm. The field has a size of 60 mm by 47 mm and

a target dose of $D_t = 5$ Gy. The planning results, which can be seen in Figure 8 for a PPP and in Figure 9 for a CPPP, exhibit a homogeneity index inside the actual target field of less than 2.5% and a gradient width of 13 mm.

4.1.2 | 'L' field

An 'L'-shaped field is more complex than the previously presented rectangular shape, consisting of two rectangular fields for which the paths can be computed in the fashion described in section 3.5. The field is comprised of two rectangular fields, one of size 60 mm by 20 mm and

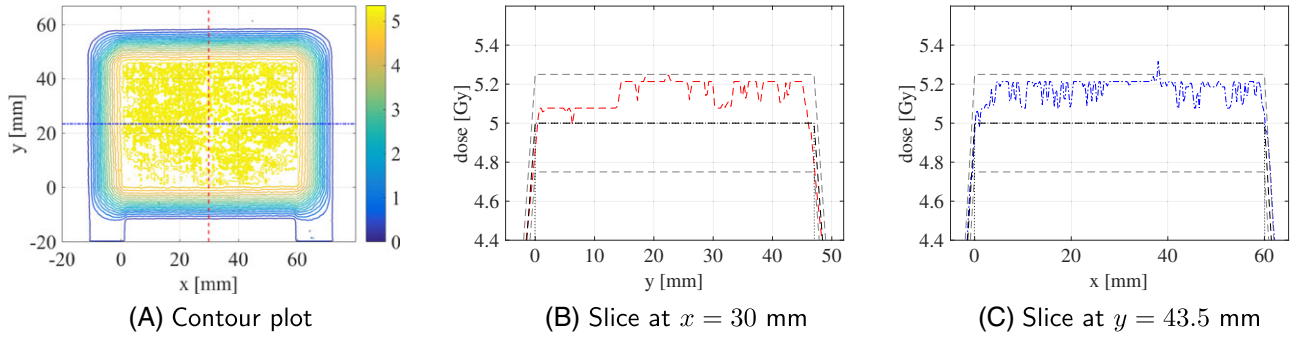


FIGURE 11 Resulting dose $D(T)$ for the executed source path as shown in Figure 8. Figures 11b and 11c show the resulting dose (red, ---) and (blue, - - -) with the target dose as shown in Figure 4b zoomed in to better show the resulting dose inside the field

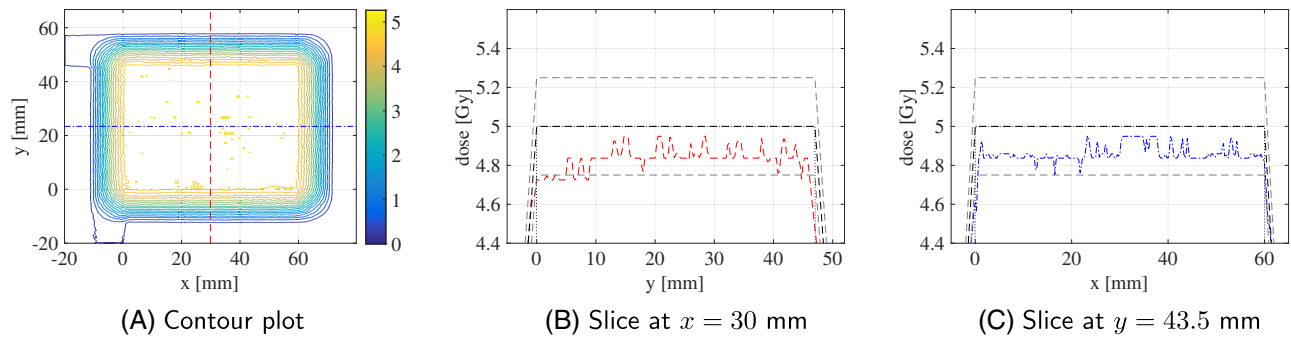


FIGURE 12 Resulting dose $D(T)$ for the executed source path as shown in Figure 9. Figures 12b and 12c show the resulting dose (red, ---) and (blue, - - -) with the target dose as shown in Figure 4b zoomed in to better show the resulting dose inside the field

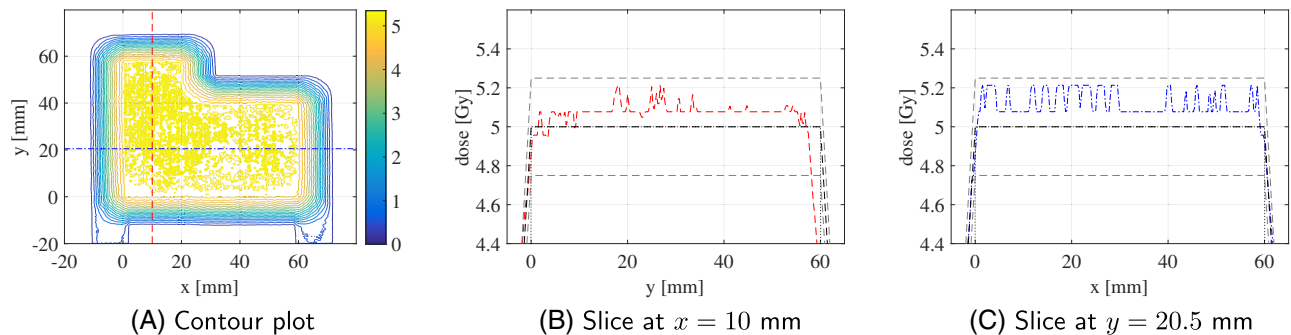


FIGURE 13 Resulting dose $D(T)$ for the executed source path as shown in Figure 10. Figures 13b and 13c show the resulting dose (red, ---) and (blue, - - -) with the target dose as shown in Figure 4b zoomed in to better show the resulting dose inside the field

one of size 40 mm by 41 mm, starting at the southeast corner of the first field. The target dose for both fields is $D_t = 5$ Gy. The planning results, which are depicted in Figure 10, were computed using a PPP and exhibit a resulting homogeneity index of less than 3% and a gradient width of 13 mm.

4.2 | Experimental results

After computation of the paths for the experimental validation of the models and the planning algorithm, the computed paths have been executed as described in section 3.6 and the measured results calibrated to absolute dose.

4.2.1 | Rectangular field

The calibrated measurement results for the rectangular fields are depicted in Figure 11 for the PPP and in Figure 12 for the CPPP. The results for the rectangular field with the PPP exhibit a mean value of 5.113 Gy and a homogeneity index of 5.012% inside the target field area. The results for the CPPP exhibit a mean value of 4.847 Gy with a homogeneity index of 4.627%. The gradient width is 13 mm for both patterns.

4.2.2 | 'L' field

The calibrated measurement results for the 'L'-shaped fields are depicted in figure 13. The results exhibit a mean value of 5.067 Gy and

TABLE 2 Mean values, standard deviation and homogeneity for the target surface dose

Field	Pattern	Results	Standard		Homogeneity index
			Mean (Gy)	deviation (Gy)	
Rectangular	PPP	planned	4.977	0.0427	2.167%
		experimental	5.113	0.0930	5.012%
	CPPP	planned	5.002	0.0461	2.352%
		experimental	4.847	0.0809	4.627%
'L' shape	PPP	planned	4.995	0.0595	2.821%
		experimental	5.067	0.1142	6.681%

a homogeneity index of 6.681% inside the target field area. The gradient width is approximately 13 mm at all edges. The mean value, the standard deviation and the homogeneity of all the results are summarized in table 2.

5 | DISCUSSION AND CONCLUSION

5.1 | Curvilinear fields and non-flat surfaces

As shown by the concept of the Riemann sum, i.e. the potentially simplest method to solve an integral, any curvilinear shape can be approximated by rectangles, with a reasonable resolution for this application. Therefore any non-rectangular field is approximated by rectangles for the purposes of this application. The approximating rectangles must comply with a lower bound for their side length. This lower bound is determined by an upper bound for the computation time and by the size of the applicator used for the radiation source. Non-planar surfaces can be approximated by planar surfaces for infinitesimal small parts of the surface. The size of the surface-parts for which this is a valid assumption is defined by the curvature of the surface. Therefore we can assume the process for planning the planar surface to be valid for non-planar surfaces as long as the radius of curvature for the non-planar surface is large enough and the planar plan is projected onto the non-planar surface for execution. Because of the reasoning presented above, we can assume that the presented planning algorithm will be able to extend the planning process to curvilinear fields on non-planar surfaces as long as the radius of curvature for both field and surface is large enough. This may be further improved by extending the planning process to non-flat surfaces and the addition of other primitives as building blocks, for instance trapezoids, for the fields.

5.2 | Discussion

When comparing the results of the planning algorithm (Figures 8 to 10) with the results of the calibrated measurements (Figures 11 to 13), it can be seen that the experimental results fit the results from the planning algorithm both qualitatively and quantitatively. However, there is a loss of accuracy between planned and experimental results.

The loss of accuracy in the experimental results can be explained by several inaccuracies of the models. These are:

- noise of the robot/source motion
- numerical noise due to discretization in time and space
- numerical noise in the source model
- inaccuracy of the calibration algorithm
- inaccuracy of the SolidWater slabs in the low-kV range
- inadequate constancy of the sources' dose output

Another issue concerns the later implementation of the system in a clinical setup. For a clinical system the robot used in this work, the LBR iiwa by KUKA, might be too expensive. But as all of the planning code is mostly independent of the robot itself, the portability to other systems should be straightforward. In order to do this, the motion model would need to be adapted to another robotic system, which can be achieved by changing the model's parameters or exchanging certain motion models if needed. The far greater issue seems to be safe interaction between the robotic system and humans, which needs to be the selection criterion for the robot to be used.

5.3 | Conclusion and future work

The study shows that target surface areas can be irradiated with acceptable homogeneity using source trajectories as calculated by the developed algorithm.

The irradiation of the fields presented here took $T = 36.4(\pm 1.2)$ minutes for each field. The irradiation of a circular area of 6 cm diameter, which represents a target area equal to the rectangular fields with a dose of $D_t = 5$ Gy, takes about 20 minutes using the surface applicator. The computation of any single field takes $t_c = 6.91(\pm 1.68)$ minutes for a PPP and $t_c = 11.43(\pm 3.74)$ minutes for a CPPP running parallelized on four Xeon E5 cores and can thus safely be assumed to be inside the margins defined in section 1.1.

A major weakness of the system in its current form is the limitation to flat surfaces. This limits medical applications to skin metastases located in flat skin areas. Non-flat surfaces, which account for most medical use cases, including intraoperative sites in sarcoma or rectal surgery, call for a system with 3D capability. If 3D capability can be implemented, the system will most likely be more accurate than any manual approach using the INTRABEAM® system. In fact, there are limited data on the actual accuracy of the routine manual approach using the INTRABEAM® system because dose distributions during surgery are not recorded and therefore the accuracy of the manual approach cannot be exactly determined. For routine clinical implementation, it will be vital to (a) determine the accuracy of IORT when an experienced radiation oncologist guides the applicator manually and (b) implement full 3D capabilities.

However, the system may be improved further by a closed loop control for the surface distance as well as by a closed loop control for the Cartesian speed based on the readings from the source's internal radiation monitor. Other improvements include the capability to use an alignment of the source that is not necessarily normal to the surface, and the ability to turn the radiation source off and on during irradiation.

With or without these changes, the next step is to demonstrate targeted radiation of a non-flat surface.



ACKNOWLEDGMENT

The authors would like to thank Gerhard Glattig for providing the Monte Carlo simulation of the radiation source. This work was funded by the German Federal Ministry for Education and Research within the Framework 'Forschungscampus: public-private partnership for Innovations' under the funding code 13GW0090 and by the European Community's Seventh Framework Program (FP7/2007-2013) for research, technological development and demonstration under grant agreement no 602306.

ORCID

Andreas Rothfuss  <http://orcid.org/0000-0002-7323-6861>

REFERENCES

- Heron M, Anderson RN. Changes in the leading cause of death : recent patterns in heart disease and cancer mortality. *NCHS Data Brief*. 2016;254:1-8.
- Fitzmaurice C, Dicker D, Pain A, et al. The global burden of cancer 2013. *JAMA Oncol*. 2015;1(4):505-27.
- National Cancer Institute [Internet]. Radiation therapy for cancer. Available from: <https://www.cancer.gov/about-cancer/treatment/types/radiation-therapy/radiation-fact-sheet>. Accessed November 25, 2016.
- Krengli M, Sedlmayer F, Calvo FA, et al. ISORT pooled analysis 2013 update: clinical and technical characteristics of intraoperative radiotherapy. *Transl Cancer Res*. 2014;3(1):48-58.
- Baum M, Vaidya JS. Targeted intra-operative radiotherapy - TARGIT for early breast cancer: Can we spare the patient daily journeys to the radiotherapist?. *Ann NY Acad Sci*. 2008;1138:132-135.
- Hohenberger P, Schwarzbach MHM. Management of locally recurrent soft tissue sarcoma after prior surgery and radiation therapy. In: Tunn PU, ed. *Treatment of Bone and Soft Tissue Sarcomas*. Berlin, Heidelberg: Springer Berlin Heidelberg; 2009:271-283.
- Sole CV, Calvo FA, Cambeiro M, et al. Intraoperative radiotherapy-containing multidisciplinary management of trunk-wall soft-tissue sarcomas. *Clin Transl Oncol*. 2014;16(9):834-842.
- Herskind C, Steil V, Kraus-Tiefenbacher U, Wenz F. Radiobiological aspects of intraoperative radiotherapy (IORT) with isotropic low-energy X rays for early-stage breast cancer. *Radiat Res*. 2005;163(2):208-215.
- Gehl J, Geertsen PF. Efficient palliation of haemorrhaging malignant melanoma skin metastases by electrochemotherapy. *Melanoma Res*. 2000;10(6):585-589.
- Moriarty JM, Xing M, Loh CT. Particle embolization to control life-threatening hemorrhage from a fungating locally advanced breast carcinoma: a case report. *Journal of Medical Case Reports*. 2012;6(1):186-191.
- Shimozuma K, Sonoo H, Ichihara K. Analysis of the factors influencing the quality of life of patients with advanced or recurrent breast cancer. *Surg Today*. 1995;25(10):874-882.
- Spratt DE, Spratt EAG, et al. Efficacy of skin-directed therapy for cutaneous metastases from advanced cancer: A meta-analysis. *J Clin Oncol*. 2014;32(28):3144-3155.
- Popescu T, Kacsó AC, Pisla D, Kacsó G. Brachytherapy next generation: Robotic systems. *J Contemp Brachytherapy*. 2015;7(6):510-514.
- Podder TK, Beaulieu L, Caldwell B, et al. AAPM and GEC-ESTRO guidelines for image-guided robotic brachytherapy: Report of task group 192. *Med Phys*. 2014;41(10):101501-101527.
- Roeder F, Krempien R. Intraoperative radiation therapy (IORT) in soft-tissue sarcoma. *Radiat Oncol*. 2017;12(1):20.
- Vaidya JS, Wenz F, Bulsara M, et al. Risk-adapted targeted intraoperative radiotherapy versus whole-breast radiotherapy for breast cancer: 5-year results for local control and overall survival from the TARGIT-A randomised trial. *The Lancet*. 2014;383(9917):603-613.
- Carl Zeiss Meditec AG [Internet]. Intrabeam XRS4;. Available from: https://www.zeiss.de/meditec/produkte/intraoperative-radiotherapie/intrabeam-system/j/m/inpagetabs{%7B}%5C_%7Dcd22/tab-13757818529/corpimage{%7B}%5C_%7D1bc2/image.mobile.980.png/1485967064541.png/zeiss-xrs-224px-263px-de.png. Accessed June 19, 2017.
- Schneider F, Clausen S, Thölking J, Wenz F, Abo-Madyan Y. A novel approach for superficial intraoperative radiotherapy (IORT) using a 50 kV X-ray source: a technical and case report. *J Appl Clin Med Phys / Am College Med Phys*. 2014;15(1):4502.
- Carl Zeiss Meditec AG [Internet]. Flat Applicator Depth Dose from 0.5mm;. Available from: https://www.zeiss.de/meditec/produkte/intraoperative-radiotherapie/intrabeam-applikatoren/j/m/inpagetabs{%7B}%5C_%7Dcd22/tab-13757818533/textimageall{%7B}%5C_%7D9af1/image.mobile.980.jpg/1477315584942.jpg/flat{%7B}%5C_%7Dapplicator{%7B}%5C_%7Dstrahlungsfeld{%7B}%5C. Accessed June 19, 2017.
- Macfarlane S, Crof EA. Jerk-bounded manipulator trajectory planning: Design for real-time applications. *IEEE Trans Robot Autom*. 2003;19(1):42-52.
- The Mathworks [Internet]. MATLAB genetic algorithm. Available from: <https://de.mathworks.com/help/gads/ga.html>. Accessed June 19, 2017.
- M2OLIE Youtube Channel [Internet]. Robotic raypainting - robotic radiation therapy (RoRaTh). Available from: <https://www.youtube.com/watch?v=ipuqkhQQ-i0>; 2016. Accessed June 19, 2017.
- Kalkan Z, Liu X, Nadrowski B, et al. A special technique for GafChromic EBT3[®] film dose calibration for low energy X-rays. In: 46. Jahrestagung der Deutschen Gesellschaft für Medizinische Physik (DGMP) e. v. Marburg, Germany; 2015:43-45.
- Kataria T, Sharma K, Subramani V, Karrthick K, Bisht S. Homogeneity Index: An objective tool for assessment of conformal radiation treatments. *J Med Phys*. 2012;37(4):207.

How to cite this article: Rothfuss A, Oesterle O, Bürgy D, et al. System and path planning algorithm for low-kV X-ray free-form surface irradiation. *Int J Med Robotics Comput Assist Surg*. 2018;14:e1899. <https://doi.org/10.1002/rcs.1899>